Title

Geophysical evidence of large-scale silica-rich fluid flow above the continental subduction interface

Authors and Affiliations

Yuantong MAO[1,2], Liang ZHAO[1,2*], Marco G. MALUSÀ[3*], Stefano SOLARINO[4], Silvia PONDRELLI[5], Baolu SUN[1], Coralie AUBERT[6], Simone SALIMBENI[5], Elena EVA[4], Stéphane GUILLOT[6]

[1]*State Key Laboratory of Lithospheric Evolution, Institute of Geology and Geophysics, Chinese Academy of Sciences, Beijing 100029, China*

[2]*College of Earth and Planetary Sciences, University of Chinese Academy of Sciences, Beijing 100049, China*

[3]*Department of Earth and Environmental Sciences, University of Milano-Bicocca, Milan 20126, Italy*

[4]*Istituto Nazionale di Geofisica e Vulcanologia, Osservatorio Nazionale Terremoti, Genova, Italy*

[5]*Istituto Nazionale di Geofisica e Vulcanologia, Sezione di Bologna, Bologna, Italy*

[6]*Univ. Grenoble Alpes, Univ. Savoie Mont Blanc, CNRS, IRD, UGE, ISTerre, Grenoble 38000, France*

*Corresponding authors (email: zhaoliang@mail.iggcas.ac.cn; marco.malusa@unimib.it

Abstract

Fluids in subduction zones can have major effects on subduction dynamics. However, geophysical constraints on the scale and impact of fluid flow during continental subduction are still limited. Here we analyze the Vp/Vs ratios in the Western Alpine region, hosting one of the best-preserved fossil continental subduction zones worldwide, to investigate the impact of fluid flow during continental subduction. We found a belt of high Vp/Vs ratios > 1.9 on the upper-plate side of the subduction zone, consistent with a partially serpentinized upper-plate mantle, and a belt of unusually low *V*p/*V*s ratios < 1.7 on the lower-plate side, at depths shallower than 30 km. We propose that these low *Vp/Vs* ratios result from a widespread network of silica-rich veins, indicating past fluid flow along the continental subduction interface. Our results suggest that past fluid flow may have reduced the effective stress along the subduction interface thus favoring continental subduction.

Key words: Western Alps, Crustal structure, Receiver function, Vp/Vs ratio, Silica enrichment

Main Text

1. Introduction

Continental subduction zones are crucial tectonic settings where the continental crust and the underlying lithospheric mantle subduct beneath the overriding plate. Seismic imaging provides direct evidence of continental subduction in many regions, such as the European Alps (Zhao et al., 2015; Zhao et al., 2016), Pamir (Schneider et al., 2013; Kufner et al., 2016), and Myanmar (Zheng et al., 2020). Exhumed (ultra)high-pressure metamorphic rocks with coesite-bearing micaschists and gneisses attest to subduction of continental crust to depths exceeding 80 km (Chopin, 1984; Liou et al., 2014). These rocks provide valuable petrologic evidence of the interaction between the slab and the surrounding mantle (Zheng et al., 2019). Fluids produced by dehydration reactions during subduction (Manning, 2004; Zheng and Hermann, 2014; Manning, 2018) are effective solvents that may favor geochemical changes and element transfers within subduction zone (Stern, 2002; Zheng and Chen, 2016). For example, serpentinites formed by the interaction of mantle rocks with slab fluids display very low effective viscosity at geological strain rates, which favors continental subduction and exhumation of deeply subducted rocks (Guillot et al., 2015; Zhao et al., 2020). In the oceanic subduction zone, fluids derived from the subducted crust may lead to silica enrichment in the forearc (Audet and Bürgmann, 2014; Hyndman et al., 2015; Halpaap et al., 2018). However, despite major efforts of the Earth science community, the scale and impact of fluid flows during continental subduction and their potential effects on subduction dynamics are still poorly constrained.

The Western Alps host one of the best-preserved fossil continental subduction wedges in the world (Guillot et al., 2009; Malusà et al., 2011). The Alpine subduction wedge was formed during progressive subduction of the Alpine Tethys and adjoining European paleomargin beneath the Adriatic microplate since the Cretaceous (Handy et al., 2010; Malusà et al., 2015). It includes rocks that were dragged to depths during subduction and subsequently exhumation, eventually being exposed east of the Frontal Pennine Fault (FPF), in the so-called Internal Zone of the Western Alps (Figure 1). The Alpine subduction wedge includes high-pressure metamorphic rocks on the upper-plate side (Eocene eclogite belt in Figure 1) and lower-pressure metamorphic rocks on the lower-plate side. The occurrence of pervasive networks of quartz veins in exhumed Alpine metamorphic rocks (Henry et al., 1996; Pettke and Diamond, 1997) provides evidence for past fluid flows and localized silica enrichment in the shallowest levels of the subduction wedge. Temporary passive seismic experiments (e.g., CIFALPS, CIFALPS-2 and AlpArray) have recently provided high-resolution velocity images based on independent geophysical methods, and attest to the subduction of European continental crust into the Adriatic upper mantle beneath the Alps (Zhao et al., 2015; Zhao et al., 2016; Lyu et al., 2017; Lu et al., 2018; Salimbeni et al., 2018; Solarino et al., 2018; Sun et al., 2019; Zhao et al., 2020; Paffrath et al., 2021; Nouibat et al., 2022; Paul et al., 2022). However, the characteristics and scale of fluid flow at greater depths remain speculative. Rocks of the subduction wedge show a wide range of seismic velocities and velocity ratios that are not necessarily correlated

(Christensen, 1996). Therefore, an integrated analysis of seismic velocities, velocity ratios (Vp/Vs) and rock densities may provide a viable tool to detect compositional variations of crustal rocks and reveal the impact of past fluid flows (Faccenda, 2014; Zheng et al., 2016).

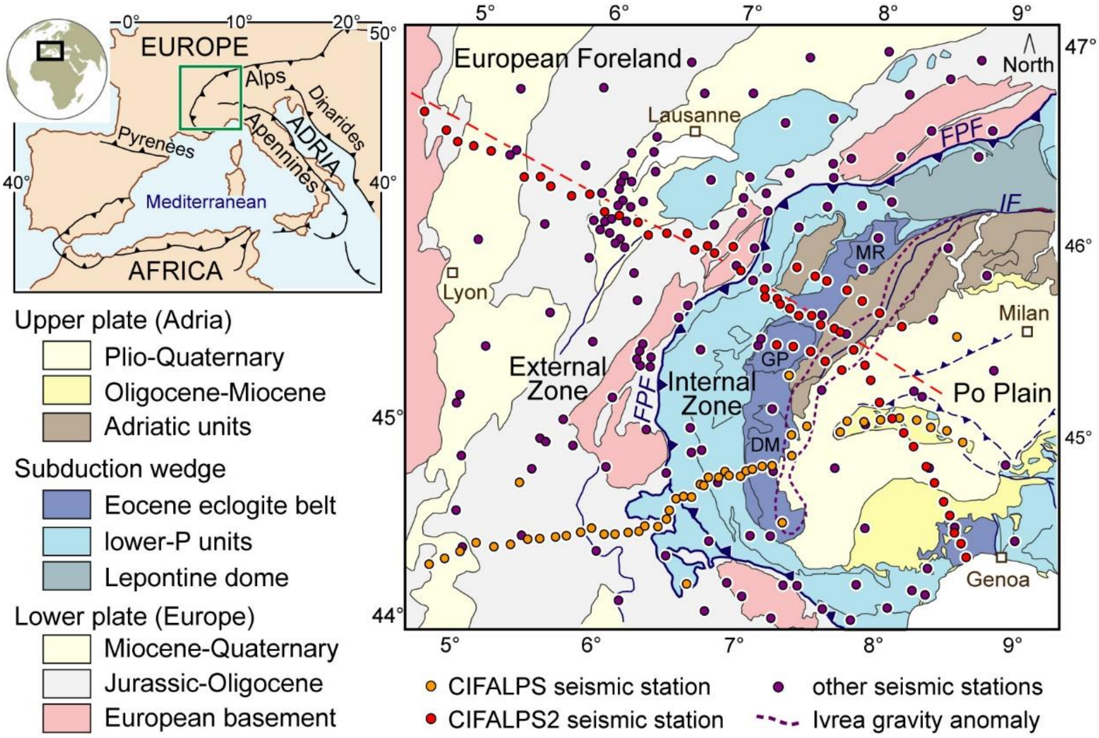

Figure 1. Geological sketch map of the Western Alps and distribution of seismic stations. The dashed red line indicates the reference profile. Acronyms: DM, Dora Maira; FPF, Frontal Pennine Fault; GP, Gran Paradiso; IF, Insubric Fault; MR, Monte Rosa (modified from Malusà et al. 2021). Ivrea gravity anomaly after Zahorec et al. (2021).

2. Data and Methods

Our study is mainly based on seismic data from the CIFALPS-2 seismic experiment, with broadband seismic stations deployed across the northern Western Alps with an average station spacing of 5–10 km (Zhao et al., 2018; Liu et al., 2022) (Figure 1), and additional data from other temporary and permanent seismic networks from 2015 to 2021, such as the CIFALPS and AlpArray experiments. To image the cross-section along the CIFALPS-2 profile, we applied receiver function analysis, 2D waveform modelling, and gravity modelling method to obtain a preferred *P*-wave velocity model and density model. To get reliable crustal average *V*p/*V*s ratios for the complex Western Alpine subduction zone, we applied an improved *H-κ-c* technique that corrects RFs for back-azimuthal variations (Li et al., 2019; Li and Song, 2021). Multiple geophysical parameters were used to conduct an integrated study on the properties of the fossil subduction zone of the Western Alps.

2.1.Observed Receiver Function Analysis

To calculate the receiver functions of CIFALPS-2 stations, a total of 67 earthquakes with magnitude Mw > 5.5 and an epicenter distance ranging from 20° to 95° were selected. We extended the selection range for teleseismic events and found a small number of valid earthquakes within the epicenter distance of 20°—30°. Each earthquake underwent careful pre-processing and manual selection. Initially, the raw seismic data were truncated to a duration of 1200 seconds, covering direct *P* waves, *Ps* waves and their multiples. We firstly downsampled all seismic sample rates to a uniform 0.02 seconds, effectively reducing the data volume. The pre-processing procedure included standard noise reduction steps such as trend removal, mean removal, and tapering. Next, the three-component recordings underwent band-pass filtering (two-pole Butterworth filter) between 0.05 Hz and 0.8 Hz. After rotation from the ZNE to the ZRT direction, we calculate the Signal-to-Noise Ratio (SNR) as the ratio of the peak amplitude of the direct *P* phase to the average amplitude across an 8-s time window prior to the onset of the *P* wave, and exclude data with SNR < 2.0 to eliminate low-quality data. A first round of visual inspection was then performed to remove the low-quality records. Bad data or data with high levels of noise are manually removed one by one. We took great care to ensure that only high-quality data were retained for subsequent analysis.

Radial RFs were then computed using the time-domain iterative deconvolution method (Ligorrfa and Ammon, 1999). To visualize the seismic structures of the CIFALPS-2 cross-section, we projected the corresponding RFs onto the profile (dashed red line in Figure 1) trending 116° from a point at 4.538°E, 46.64°N. A total of 2541 high-quality radial receiver functions were obtained after a second round of visual inspection to remove low-quality receiver functions. We adopted the simple and yet powerful approach referred to as the "Common Conversion Point" (CCP) stack method (Zhu and Kanamori, 2000) to migrate RFs from the time domain to the depth domain. A high-resolution *S*-wave velocity model from ambient noise tomography (Nouibat et al., 2022) was used as the local lithosphere velocity model for time-depth migration, and the classical crustal *Vp/Vs* ratio of 1.73 was utilized. The space beneath the array was divided into bins at intervals of 0.1 km in the vertical direction and 1 km in the horizontal direction. We averaged the migrated amplitudes contributing to each individual bin only if the number of receiver functions in a bin was no less than 10. All the migrated receiver functions within 35 km were projected onto our profile and stacked. Horizontal smoothing was then applied using a half-width Gaussian operator, increasing linearly with depth from 7 km at the surface to 15 km at 30 km depth. Finally, a CCP depth cross-section was obtained.

The waveforms of RF strongly depend on the event back-azimuths, yielding different CCP images for different ranges of back-azimuths (Figure 2) (Cassidy, 1992). Because we are most interested in the geometry structures along the profile and we need to remain consistent with our 2D waveform modelling, we selected events with back-azimuths of 71°–161° and 251°–341° to minimize the effects of the 3D structure.

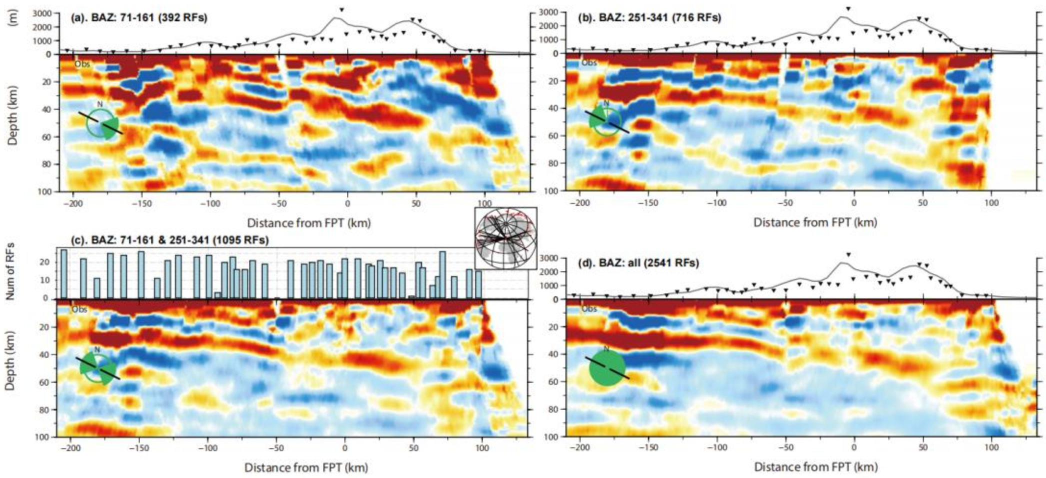

Figure 2. CCP depth sections computed from events for different back-azimuths. Ranges of back-azimuths are indicated by the green pies or circles. The black line across the circle indicates the strike of the profile. (a) ESE back-azimuths (71°–161°). (b) WNW back-azimuths (251°–341°). (c) Both sides of the profile (71°–161° and 251°–341°). The number of individual receiver functions stacked for each station is given in the bar plot. Inset shows the events distribution. Red dots represent all the events, and among them, the red dots connected by black solid lines are the events used during CCP stacking. (d) All back-azimuths.

2.2. *H*-*κ*-*c* stacking technique

The RF technique enhances *Ps* waves on velocity interfaces, especially for strong velocity interfaces such as the Moho (Ammon et al., 1990). The traditional *H*-*κ* stacking technique using teleseismic RFs to obtain the crustal thickness and average *V*p/*V*s ratio is based on the assumption of a horizontally layered isotropic model (Zhu and Kanamori, 2000). It stacks RF amplitudes at predicted *Ps* conversion and crustal multiples (*PpPs* and *PpSs* + *PsPs*) for a given *H* and *κ*. *H* denotes the depth of the strongest velocity interface, typically referring to the crustal thickness; *κ* denotes the average *V*p/*V*s ratio between the velocity interface (such as Moho) and the surface. Compared to the CCP stacking method, which only utilizes the *Ps* conversion, the *H-κ* method also employs its multiples to constrain the crustal structure and average *V*p/*V*s ratio. Due to the trade-off between *H* and *κ*, constraining solely with *Ps* conversions would result in a range of *H* and *κ* outcomes. However, by stacking RF amplitudes of multiples, a concentrated energy cluster is obtained, allowing for the unique determination of *H* and *κ*.

The *H-κ-c* is an enhanced *H-κ* technique that includes harmonic corrections on *Ps* and its crustal multiples, which could minimize the effects of crustal anisotropy and dipping interfaces (Li et al., 2019). *c* stands for the correction for the azimuthal variation of arrival times of *P*s and its crustal multiples. Systematic synthetic tests show that the arrival time variations of *Ps* and its multiples can be well fitted by *cosθ* and *cos2θ* functions even for very complex crustal structures. The equation for the harmonic fitting is

$$F(\theta) = A_0 + A_1 \cos(\theta - \theta_1) - A_2 \cos 2(\theta - \theta_2)$$

where $F(\theta)$ represents the variation of arrival times with back-azimuth (θ) for *Ps* or crustal multiples, A_0 is the central arrival time, and A_1, A_2, θ_1, and θ_2 are the amplitudes and phases of the two-lobed and four-lobed variations (Li et al., 2019). *H-κ-c* includes four main steps: 1) traditional *H-κ* stacking to calculate the reference arrival times for *Ps* and multiples; 2) incidence moveout correction and 5-degree back-azimuthal binning; 3) harmonic analysis around reference arrival times to obtain the harmonic parameters, it applied a simple grid search method to search for the most fitted parameters; and 4) harmonic corrections and new *H-κ* stacking with the corrected RFs. Our search range for average *V*p/*V*s ratio was limited to 1.6–2.1. And follow the parameters from Li et al. (2019, 2021), the weighting of *Ps* and multiples was 0.5, 0.4 and 0.1.

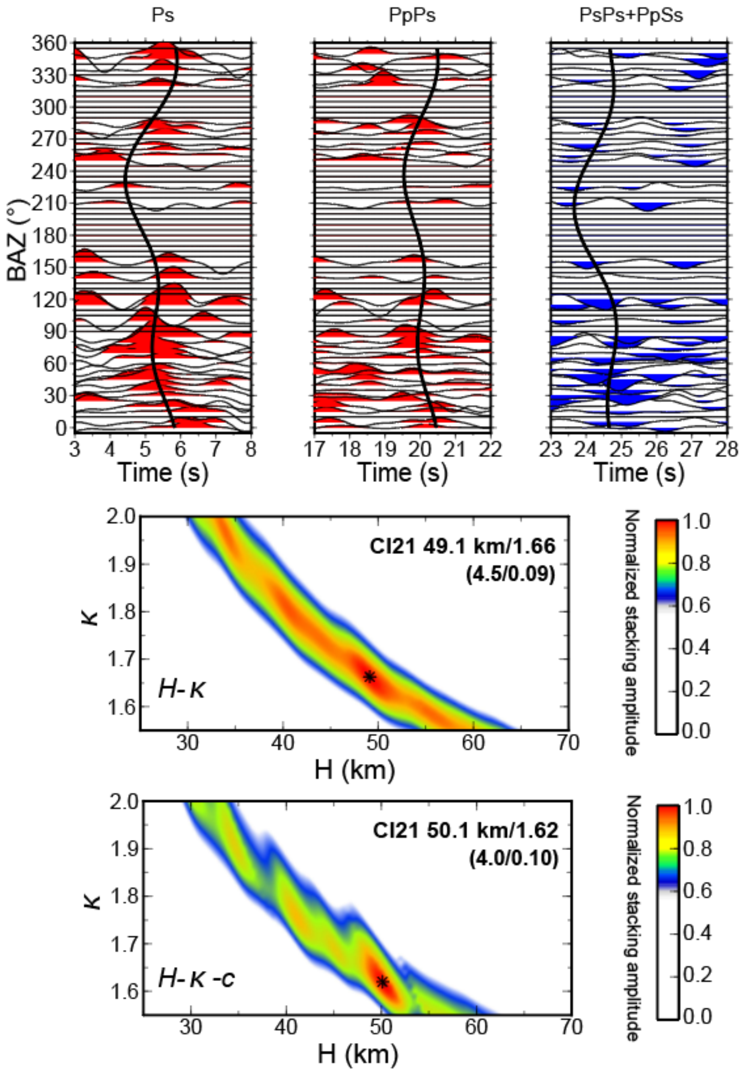

Figure 3. Radial receiver functions and *H*-κ-*c* stacking for station CI21. The top panels show harmonic fitting results for *Ps*, *PpPs* and *PsPs*+*PpSs*. The harmonic fitting for *Ps* and multiples are shown as black solid lines. *H*-κ stacking before and after the harmonic corrections are show at bottom. The obtained *H* and κ values, and their standard deviations are presented on the stack diagrams. The preferred point in the energy map represents the obtained *H* and κ.

The harmonic corrections among the three arrivals (*Ps*, *PpPs* and *PsPs*+*PpSs*) are variable. Theoretically, the crustal anisotropy and dipping interface could both contribute to the arrival time variations of *Ps* and its crustal multiples. Synthetic tests show that the effect of azimuthal anisotropy on multiples is almost the same as on *Ps*, while the effect of a dipping Moho on multiples is about 5 times of that on *Ps* (Li et al., 2019). So it's hard to say whether the multiples have larger or smaller variations than *Ps* conversion. Besides, the subduction complex is strongly laterally heterogeneous. It is still challenging to separate the combined effects of anisotropy and dipping interface, as well as their combined impact on the travel times variations of *Ps* conversions and multiples. In this work, considering the great complexity of the Western Alps, we judiciously decided not to use the harmonic fitting parameters for additional interpretations of crustal anisotropy and dipping interfaces.

H-κ-c usually provide more accurate picks of converted phases and stronger stacking energy cluster than *H-κ* results. In Figure 3, the harmonic fitting for *Ps* and multiples are shown as black solid lines. The harmonic corrections enhance the accuracy of arrival times of *Ps* and multiples. Therefore, the stacking energy should be more concentrate and stronger on the predicted arrival times after applying the harmonic corrections. For most of the stations in the Western Alps, running through *H-κ-c* steps once was sufficient, but special care was required. The traditional *H-κ* method provides reference arrival times for *Ps* and multiples, which can help narrow down the search range for conversions. Strong signals caused by sediment, on the other hand, may result in an incorrect search range (for example, a *Ps* signal before 2 s). However, considering our previous findings in this region and the CCP depth images, we can constrain the Moho depth to a specific range. Figure 4 illustrates a typical example. Before manual adjustment, the waveforms were interfered by shallow sediments, and the conversions were identified around 2–3 seconds. But based on prior results and our CCP depth images, the Moho depth beneath station CI19 is around 35 km, suggesting that the *Ps* wave arrival time should be later. We limited the search range for the *Ps* conversion wave and recalculated the *H-κ-c*. After a manual update of reference arrival times based on the CCP depths and redoing the above steps, the *Ps* arrival time should be corrected for most cases where the *Ps* is clearly distinguished from other noise signals (Figure 4, CI19). Then, by visually examining the morphology of each energy cluster individually, including its concentration and uniqueness, we were able to make a preliminary assessment of the reliability of the stacking results. Stations with insufficient back-azimuthal coverage of high-quality RFs (e.g., CI14) or poor signal-to-noise ratios (e.g., CI29, CI31–CI33) are removed. Due to the trade-off between crustal thickness and average *V*p/*V*s ratio, we examined the crustal thickness in the study region by comparing it with the Moho depths independently obtained from CCP depths and other previous tomography studies (Nouibat et al., 2022; Paul et al., 2022). By utilizing these approaches, we furtherly validated the reliability of the average *V*p/*V*s ratio results. However, we should note that the *H-κ-c* method shares the same fundamental principles as the traditional *H-κ* method. While applying the *H-κ-c* method may yield more accurate picks, it may not significantly affect our major conclusions. For example, in Figure 3, the harmonic fitting for *Ps* and multiples exhibits little variations (within 1 second). After corrections, the stacking energy is more concentrated. However, compared to the traditional *H-κ* method, the improved results show no qualitative changes.

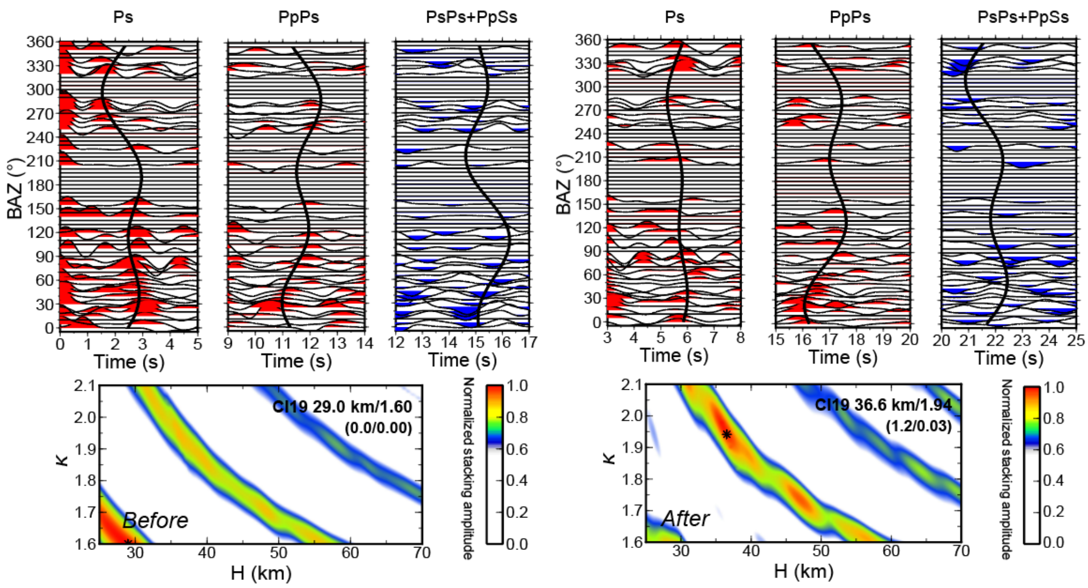

Figure 4. Radial receiver functions and *H-κ-c* results for station CI19 before and after manual adjustment. The left panels show harmonic fitting RFs and *H-κ-c* stacking results before manual adjustment. The right panels show harmonic fitting RFs and *H-κ-c* stacking results after manual adjustment. The preferred point in the energy map represents the obtained *H* and *κ*.

2.3. Receiver Function and Gravity Modelling

To image the crustal velocity and density of the CIFALPS-2 cross-section, we used a 2D modelling method to simulate the RFs and Bouguer gravity anomaly. The initial structural model for forward modelling was first obtained from ambient noise tomography, providing the basic principle of structural division. Secondly, combined discussions with geological studies of western Alps, the structure within 10 km is also finely depicted in Figure 5a (Paul et al., 2022) (Figure 5a). Our CCP depth section also contributed to the Moho geometry of initial model. Finally, the crustal geometry used for forward modeling is illustrated in Figure 5b.

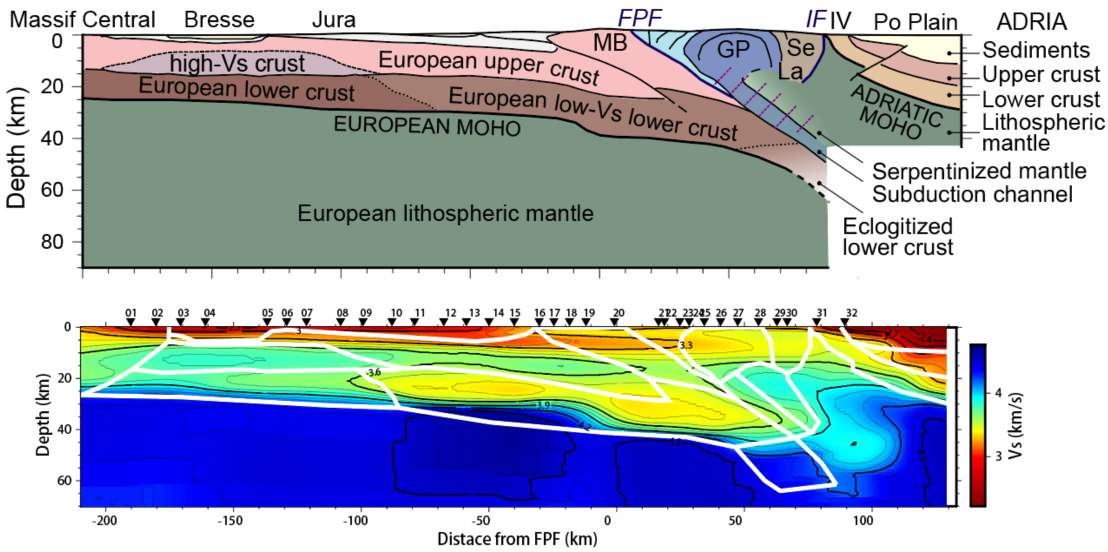

Figure 5. Initial model for gravity and RF waveform modelling. Initial model from geological interpretation (top panel, image from Paul et al., 2022) and S-wave velocity image from ambient noise tomography (bottom panel, data from Nouibat et al., 2022). The crustal

structure lines (white solid lines in Figure 5b) we used for forward modelling were initially drawn based on the geological map in Figure 5a, incorporating information from S-wave velocity image and geological interpretations. And minor adjustments to the Moho interface were made based on our CCP depth images.

In forward RF modelling, the initial *P*-wave velocity model was calculated from the *S*-wave velocity model from ambient noise tomography (Nouibat et al., 2022)(Figure 5). The average *S*-wave velocity was first obtained from the *S*-wave model, and the corresponding *P*-wave velocity was calculated based on a *V*p/*V*s ratio equal to 1.73. We computed synthetic RFs using a 2D hybrid waveform modelling method (Zhao et al., 2008; Zhao et al., 2015). The spectral element method (SEM) (Komatitsch and Tromp, 1991) was applied for the local initial model, while the generalized ray theory (GRT) (Wen and Helmberger, 1998) was utilized externally where the global velocity model was set as Preliminary Reference Earth Model (PREM) (Dziewonski and Anderson, 1981). Then, a synthetic CCP image was computed using the same deconvolution and migration methods as for the observed CCP image. Finally, we adopt an iterative process to update the *P*-wave velocity model by minimizing the misfit between the synthetic CCP cross-section and the observed CCP cross-section.

For gravity modelling, density-velocity empirical relationship formulas (Ludwig et al., 1970; Perrier and Ruegg, 1973; Brocher, 2005; Reynard, 2013) were used to calculate the initial density model. The simple linear relationship ($Vp = 3.85\rho - 4.81$) is used on the sedimentary part (when *V*s <= 3 km/s), the Nafe-Drake relationship ($V_P = 39.128\rho - 63.064\rho^2 + 37.083\rho^3 - 9.1819\rho^4 + 0.8228\rho^5$); on the crust part and the Reynard relationship ($Vp = 3.636\rho - 4.109$) on the mantle part (when *V*s >= 3.90). Bouguer gravity anomaly data were extracted from the latest dataset of the AlpArray Gravity Working Group (Zahorec et al., 2021). The 2D gravity forward modeling method can be used to calculate synthetic gravity anomalies based on a crustal density model (Talwani et al., 1959). Then a series of forward modeling were adopted and the density model was iteratively updated, by improving the fit between synthetic Bouguer gravity anomalies and observed Bouguer gravity anomalies.

3. Results

3.1. Average *V*p/*V*s ratios in the Western Alpine

The crustal thickness and average *V*p/*V*s ratios results are presented in Figure 6. The results of average thickness and *Vp/Vs* ratios, together with their standard derivations are listed in Table S1. The *H-κ-c* method provides a total of 198 good results with smaller errors in the Western Alps region, as well as the CIFALPS-2 profile (Figure S1-S3).

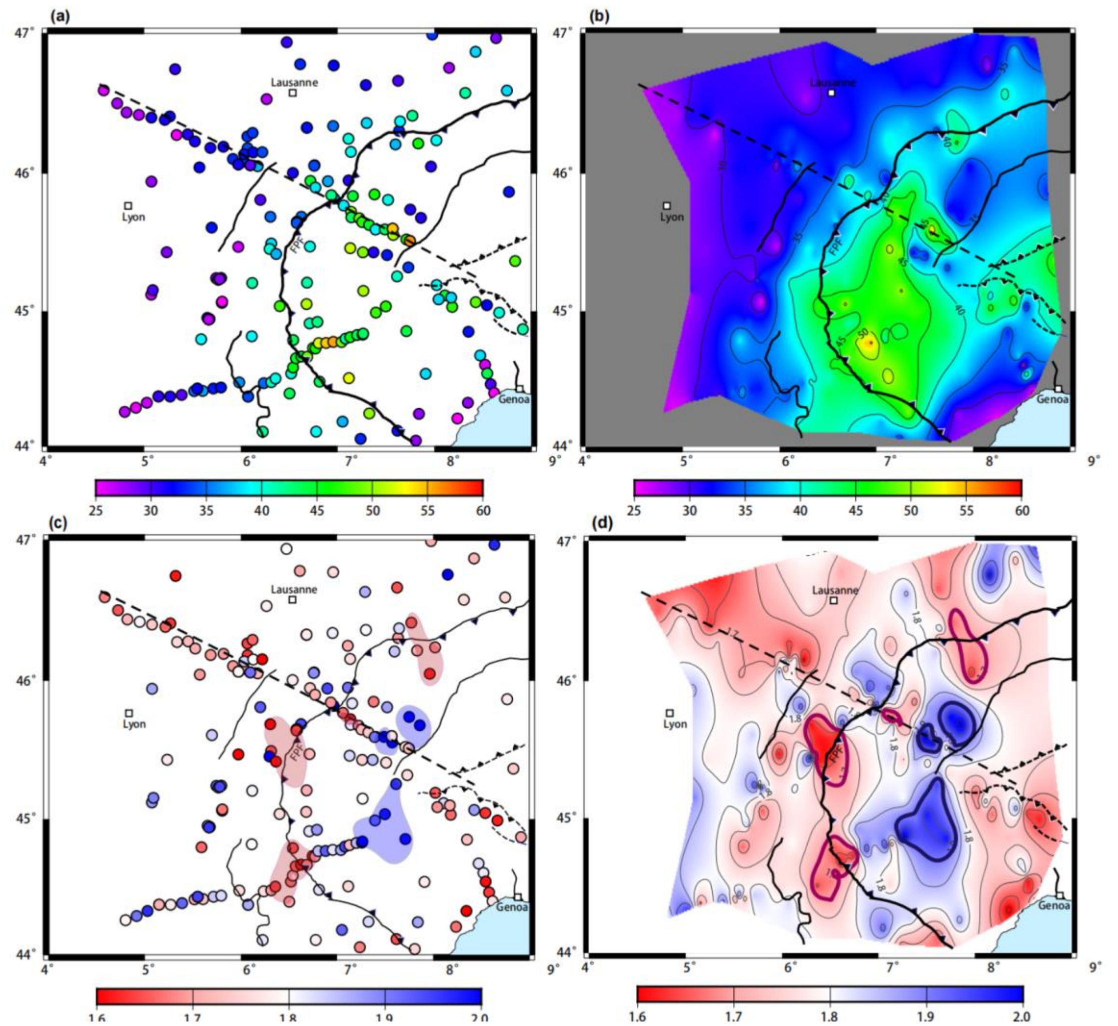

Figure 6. *H*-*κ*-*c* results in the Western Alpine region. (a) Scatters of crustal thickness. (b) Interpolated results of crustal thickness. (c) Average *V*p/*V*s ratios for single stations. The red shadowed areas represent the regions where the contour of *V*p/*V*s is less than 1.7, while the blue shaded represent areas where the contour is greater than 1.9. (d) Interpolated results of average *V*p/*V*s ratios. Black dashed line indicates the CIFALPS-2 profile. Major faults are also shown for reference.

In the Western Alps subduction wedge, low *V*p/*V*s values (< 1.7) are observed in the vicinity of the Frontal Pennine Fault, whereas high *V*p/*V*s values (> 1.9) are found on the upper-plate side of the subduction zone, 50 to 100 km to the east of the Frontal Pennine Fault. Low *V*p/*V*s values characterize the European Foreland to the NW, where slightly higher *V*p/*V*s ratios also define a NE-SW belt that may suggest compositional changes likely inherited from the pre-Alpine evolution of the European crust. This NE-SW belt is consistent with the trend of NE-SW Moho steps revealed by independent geophysical methods (Malusà et al., 2021; Paul et al., 2022), and with the trend of the European paleomargin inferred from independent geological data (Malusà et al., 2016; Ji et al., 2019). In the Adriatic upper plate, the average crustal *V*p/*V*s values are more homogeneous and generally lower than 1.8.

Figure 7 also shows the *H-κ-c* cross-section along the CIFALPS-2 profile. In Figure 7b, the gray solid line represents the Moho interface from the CCP depth cross-section, while the red dots with blue bars represent the velocity interface thicknesses *H* and their standard deviations. In the European Foreland, the crustal thicknesses *H* agree with our CCP depths and other published Moho depths based on geophysical datasets (Nicolas et al., 1990b; Spada et al., 2013; Nouibat et al., 2022; Paul et al., 2022). However, in the subduction complex of the 50–70 km distance range, it can be seen that two distinguishable *Ps* conversions exist at approximately 45 km, and 65 km depths, respectively (Figure 8d). The *Ps* conversions at a depth of ~65 km (solid gray line) remain strong and consistent from CCP images of events from different back-azimuth, which suggests that the European slab subducted to deeper depths. On the other hand, the *Ps* conversions at a depth of ~45 km (dashed gray line) correspond to the crustal structure interface extracted from the ambient noise tomography, which represent the strong velocity interface between normal-crust and partially eclogitized European lower crust. In contrast to the CCP stacking technique, the *H-κ-c* method not only utilizes *Ps* conversions, but also incorporates multiples to constrain the average velocity ratio above interfaces. In this complex region, the velocity interface calculated by the *H-κ-c* method falls around 45 km, consistent with the 45 km interface obtained by CCP stacking technique. However, it is important to note that this interface does not correspond to the Moho boundary. Hence, the associated *κ* values do not represent the average crustal velocity ratios but rather the average velocity ratios above specific eclogitized European lower crust interfaces.

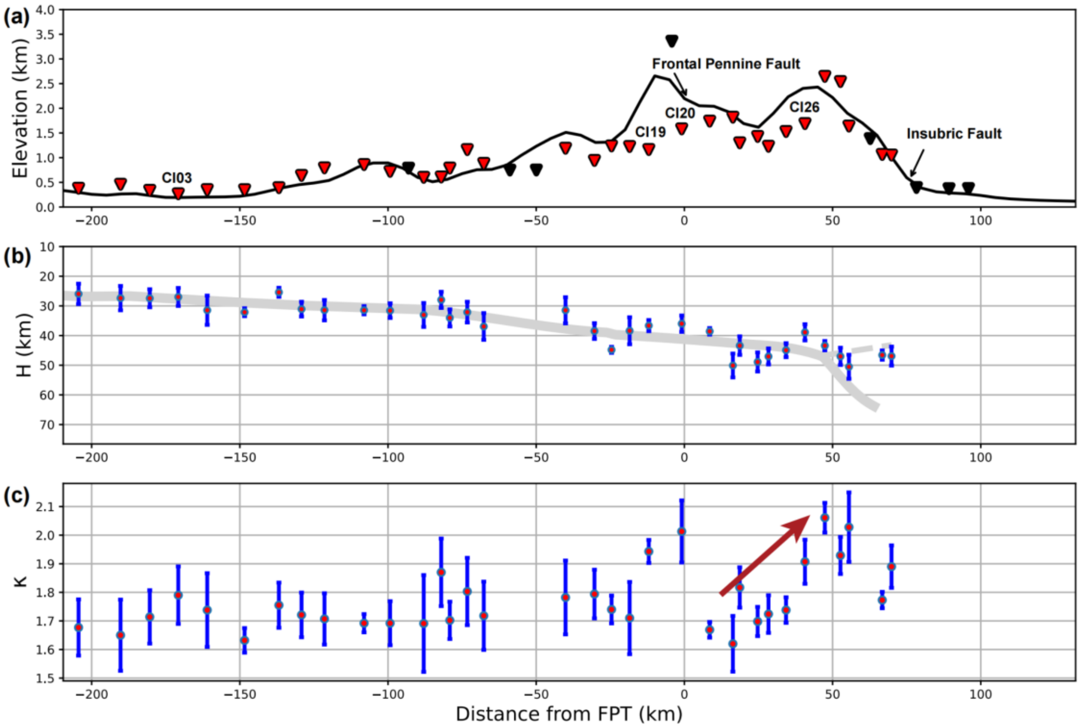

Figure 7. *H*-*κ*-*c* results of CIFALPS-2 vertical cross-section. (a) Topography with seismic stations of CIFALPS-2. Red triangles represent stations with available *H*-*κ*-*c* results. (b) Depths of strong velocity interface (*H*) with standard deviations (blue error bar). The gray line represents the Moho geometry from our CCP cross-section, where the dashed gray line represents the velocity boundary between the European crust and partially eclogited crust. (c) Average *V*p/*V*s ratios (*κ*) with standard derivations. The red arrow indicates a gradual increase in *V*p/*V*s ratios.

The average *V*p/*V*s ratios above the calculated interfaces are shown in Figure 7c. The European foreland has average *V*p/*V*s values of ~1.70. However, the presence of sedimentary successions, for example beneath station CI03, may locally increase the crustal average *V*p/*V*s ratio. Moving eastward to the Jura mountains (–90 km – –50 km), average *V*p/*V*s values are slightly higher and with larger standard deviations. The *V*p/*V*s ratio of CI19 and CI20 does not show consistent continuity with the surrounding stations, and we attribute this observation to structural effects in terms of diffuse fracturing along this major crustal fault. However, an extensive discussion of this issue is beyond the aims of this paper. We openly acknowledge a challenge in our current study, namely that although the standard deviation of *H-κ-c* has been significantly reduced, it remains relatively high in complex regions, especially for *Vp/Vs* (Figure S1). Although there are instances where the standard deviation may be large, indicating dispersed energy, the point with the highest energy still holds significance as a reference. Our focus is analyzing the lateral variations in the *Vp/Vs* ratio, especially on the subduction zone. Taking into account the errors, the results of this lateral profile, CIFALPS-2, exhibit similarities within the range of approximately −200 to 40 km, while also displaying notable variations within the subduction zone in the 0–100 km range. The variations make us speculate the possible existence of the anomaly in the subduction zone. Moreover, by integrating the results from the entire Western Alps, we can further infer a continuous anomaly along the subduction zone. Besides, the average *Vp/Vs* ratio in the frontal European continental part of profile is also low. We did not delve into its nature in this work. This cross-section result in the subduction zone indicates that associated *V*p/*V*s anomalies should come from rocks not deeper than 45 km, even though the slab has already subducted to greater depths.

3.2. Vertical Cross-sections for CIFALPS-2

To further study the depth of the *V*p/*V*s anomalies, we calculated preferred density and *P*-wave velocity models along the CIFALPS-2 profile. The observed CCP depth section (Figure 2) is slightly different from the previous ones (Paul et al., 2022) due to the different back-azimuths considered for the stacking. In this study, we chose seismic events from both sides of the profile to ensure a distribution that aligns better with the requirement of two-dimensional waveform modelling. The European Moho was continuously detected from ~25 km depth at the western end of the profile to ~45 km depth beneath the Gran Paradiso dome (GP in Figure 1). A weak but reliable conversion ascribed to the European Moho, which is observed in cross-sections with different back-azimuths, reaches a maximum depth of ~65 km beneath the Insubric Fault (IF in Figure 1), where the Bouguer gravity anomaly shows a long-recognized maximum due to lower crustal and mantle rocks exhumed to shallow depths (Zahorec et al., 2021).

Figure 8 also displays the cross-sections of the preferred *P*-wave velocity and density models. The distribution trends of density and velocity on this cross-section are similar, implying that regions with higher density correspond to areas with higher velocity. Given the use of the diverse techniques and raw data sources, our focus lies on the relative parameters among different blocks rather than the absolute values. The subducted European lower crust shows high *V*p values (6.71 km/s) and low *V*s values (Figure 5b), which implies high *V*p/*V*s ratios. Above the subducted lower crust, the *V*p for lower-pressure metamorphic frontal wedge and eclogitized belt are 5.81 km/s–5.88 km/s, which implies much lower *V*p/*V*s ratios compared to the European lower crust. This result suggests that the unusually low average *V*p/*V*s anomalies revealed by the *H-κ-c* method should originate from the Internal zone, with depths shallower than 30 km.

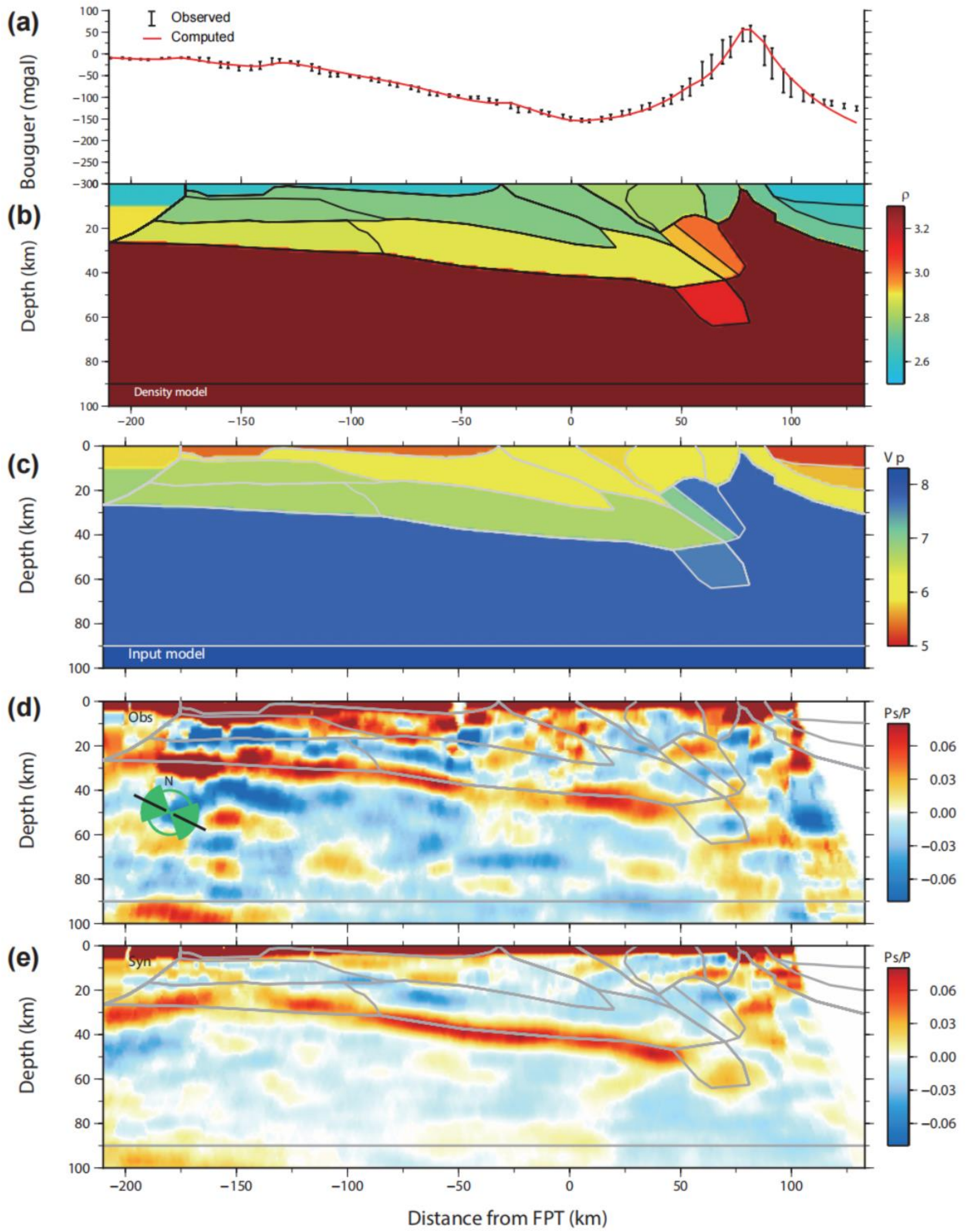

Figure 8. Common conversion point (CCP) cross-section and *P*-wave velocity model projected onto the reference profile. (a) Observed and computed Bouguer gravity anomaly. (b) Preferred density model. (c) Preferred *P*-wave velocity model. (d) Observed CCP migrated depth section computed from teleseismic events. (e) Synthetic CCP migrated depth section.

4. Discussion

4.1. *V*p/*V*s anomalies in subduction zones

The average *V*p/*V*s ratio is commonly considered as a key constraint on the nature and composition of rocks. Laboratory measurements show that *V*p/*V*s ratio is more sensitive to compositional variations, but much less sensitive to temperature and pressure variations (Christensen, 1996; Lowry and Perez-Gussinye, 2011). The *V*p/*V*s ratios for different rock types forming the continental crust and possibly involved in continental subduction generally range between 1.72 and 1.85 (Carmichael, 1989; Christensen, 1996), see in Figure 9. Notably, many other factors could influence the *V*p/*V*s ratio, such as fluids/melts, and anisotropy. The presence of fluids/melts can increase the *V*p/*V*s ratio of crustal rocks by lower the *S*-wave velocity. Nonetheless, it is not anticipated that active fluid flows or melts would occur in the fossilized subduction wedge of the Western Alps, as subduction has ceased to be active for at least 30 Ma. Petrological studies have also shown that the anisotropy of peridotite may decrease the *V*p/*V*s ratio under high-pressure and high-temperature conditions (at depths of 90–120 km and temperatures above 800°C) (Hacker and Abers, 2012). In our study, the average *V*p/*V*s ratios are obtained by stacking the receiver function waveforms from all back-azimuths, which allows us to greatly reduce the influence of anisotropy. Moreover, as referenced in Section 3.2, low *V*p/*V*s anomaly in Western Alps in this study is located above 30 km, and the high *V*p/*V*s anomaly is located above 45 km. Hence, we can preliminarily exclude the influence of anisotropy on the average *V*p/*V*s ratios.

*V*p/*V*s ratios are generally high for serpentinite (2.0–2.2), and the occurrence of average *V*p/*V*s ratios as high as ~2.0 on the upper-plate side of the subduction zone is therefore consistent with the presence of a partially serpentinized upper mantle of Adriatic plate possibly lying on top of a serpentinized subduction channel, as suggested by previous work (Zhao et al., 2020; Malusà et al., 2021). Our results may suggest the presence of hydrated serpentinite or partially hydrated serpentinite above the 45 km depth in high-pressure subduction zones.

The occurrence of very low *V*p/*V*s values along the Frontal Pennine Fault is instead a new finding of this study. As shown in Figure 9, *V*p/*V*s ratios are very low for quartz (1.46–1.48). Other structural or compositional changes are unlikely to generate such low *V*p/*V*s anomalies. Considering the widespread presence of quartz veins observed on the surface of the Western Alps, as outlined in the Introduction, we hypothesize that an extensive network of quartz veins may significantly reduce the average *V*p/*V*s ratio of the host rock.

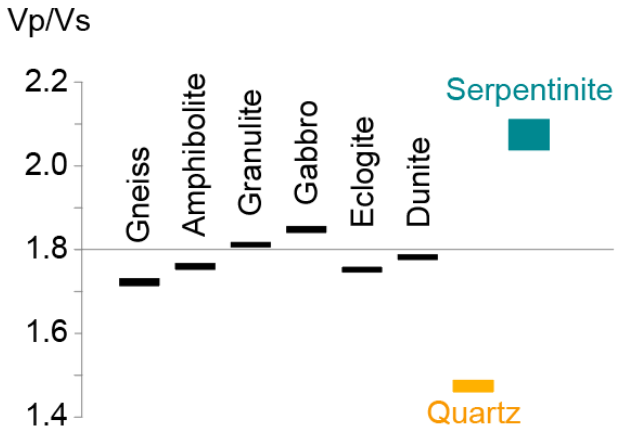

Figure 9. Laboratory *V*p/*V*s ratios for different rock types at 1000 MPa. *V*p/*V*s ratios generally range between 1.72 and 1.85 (black boxes), but they are much lower for quartz (1.46–1.48) and much higher for serpentinite (2.0–2.2). (data after Carmichael, 1990 and Christensen, 1996)

4.2. Implications on continental subduction

We thus speculate that the low *V*p/*V*s ratios here documented in the Internal zone reveal past silica-rich fluid flows that occurred when subduction was still active, as now attested by the presence of a pervasive network of quartz veins. High temperatures are required for quartz to dissolve in pure water. Our conceptual model (Figure 10) does not strictly adhere to the depth proportions of the actual CIFALPS-2 profile in Figure 8. Instead, it utilizes temperature isotherms. The silica-enriched zone is situated above the average crustal depth (< 30 km), exhibiting similar temperature and pressure conditions to the average crust.

The fluids responsible for the formation of quartz veins were likely generated through dehydration reactions of subducted slab during the subduction process and subsequently ascended along the subduction channel. As the oceanic slab and continental slab subduct into the mantle, hydrous minerals are breakdown and fluids are released from the slab with increasing temperature and pressure (Zheng and Hermann, 2014). With a relatively high solubility at high temperature, silica is a major solute in fluids (Hermann et al., 2013). The solubility of silica is favored by the presence of salts and CO_2 (Audétat and Keppler, 2005; Rapp et al., 2010; Hunt and Manning, 2012; Li et al., 2020). When the continental crust reaches mantle depths, the temperature often exceeds 600 °C (Wang et al., 2021), which is high enough for silica to be largely dissolved into fluids. At deeper depth, fluids may exist in a form of a supercritical state, which would furtherly enhance the solubility for the silicate minerals (Manning, 2004; Cruz and Manning, 2015; Ni et al., 2017; Chen et al., 2018). In active subduction settings, these fluids can migrate easily upwards along an impermeable plate interface (Halpaap et al., 2018). As these silica-rich fluids ascend along the subduction interface, a decrease in pressure and cooling lead to a decrease in quartz solubility, resulting in the deposition of quartz, as exemplified by the presence of quartz veins in the Western Alps. Consequently, the large-scale silica may be gradually frozen above the subduction interface. Therefore, we posit that the quartz vein network observed in exposed Alpine rock formations (Henry et al., 1996; Pettke and Diamond, 1997; Tricart et al., 2004) merely represents a lower limit of the conditions we envision at greater depths based on geophysical evidence. However, further analyses based on geophysical methods are required to prove such hypothesis.

Scientists have also documented anomalously low *V*p/*V*s ratios, interpreted in terms of silica enrichment, above the subduction interface of some major oceanic subduction zones, for example in the Hellenic, North Cascadia and Mexico, (Huesca-Pérez and Husker, 2012; Audet and Bürgmann, 2014; Hyndman et al., 2015; Halpaap et al., 2018). Our work in Western Alps is the first to proposes a silica-enrichment in a fossil continental subduction zone. However, we find that similar geophysical features are also observed in the Himalaya (Li and Song, 2021), where average *V*p/*V*s ratios sharply decrease to the north of the Main Frontal Thrust and Main Boundary Thrust, and in the Zagros, which also show low crustal average *V*p/*V*s ratios in subduction zone (Shiranzaei et al., 2021). These studies may indicate that silica enrichment could be a common occurrence in both oceanic and continental subduction zones.

Zhao et al. (2020) suggest that due to the low viscosity at geological strain rates of serpentinite, serpentinization above subduction interfaces may facilitate continental subduction and exhumation. In this study, the presence of silica-rich materials in the upper part of the subduction zone suggests the occurrence of previous fluid flow along the subduction interface. This fluid flow could have diminished the effective stress along the subduction interface, thereby also significantly promoting the process of continental subduction.

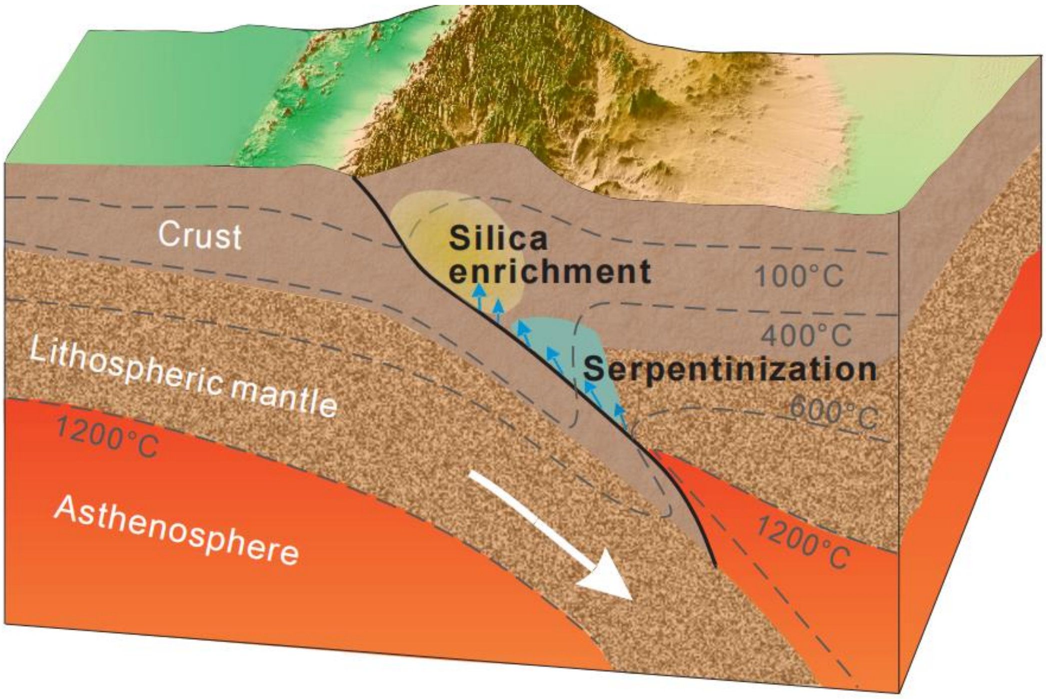

Figure 10. Conceptual model of silica enrichment and serpentinization in the subduction zone. Fluids are released from the slab as temperature and pressure rise. Some fluids combine with the mantle wedge, producing hydrous serpentinites; parts of silica-rich fluids flow upwards along the subduction interface, leading to silica enrichment above the subduction interface.

References

Ammon C J, Randall G E, Zandt G. 1990. On the nonuniqueness of receiver function inversions. J Geophys Res, 95: 15303–15318

Audet P, Bürgmann R. 2014. Possible control of subduction zone slow-earthquake periodicity by silica enrichment. Nature, 510: 389–392

Audétat A, Keppler H. 2005. Solubility of rutile in subduction zone fluids, as determined by experiments in the hydrothermal diamond anvil cell. Earth Planet Sci Lett, 232: 393–402

Brocher T M. 2005. Empirical Relations between Elastic Wavespeeds and Density in the Earth's Crust. Bull Seismol Soc Amer, 95: 2081–2092

Carmichael R S. 1989. Practical Handbook of Physical Properties of Rocks and Minerals. Physical properties of rocks and minerals. Boca Raton: CRC Press.

Cassidy J F. 1992. Numerical experiments in broadband receiver function analysis. Bull Seismol Soc Amer, 82: 1453–1474

Chen W, Xiong X, Wang J, Xue S, Li L, Liu X, Ding X, Song M. 2018. TiO_2 solubility and Nb and Ta partitioning in rutile-silica-rich supercritical fluid systems: Implications for subduction zone processes. J Geophys Res: Sol Ea, 123: 4765–4782

Chopin C. 1984. Coesite and pure pyrope in high-grade blueschists of the Western Alps: a first record and some consequences. Contrib Mineral Petr, 86: 107–118

Christensen N I. 1996. Poisson's ratio and crustal seismology. J Geophys Res, 101: 3139–3156

Cruz M F, Manning C E. 2015. Experimental determination of quartz solubility and melting in the system SiO_2–H_2O–NaCl at 15–20 kbar and 900–1100 °C: implications for silica polymerization and the formation of supercritical fluids. Contrib Mineral Petr, 170: 35

Dziewonski A M, Anderson D L. 1981. Preliminary reference Earth model. Phys Earth Planet In, 25: 297–356

Faccenda M. 2014. Water in the slab: A trilogy. Tectonophysics, 614: 1–30

Guillot S, Hattori K, Agard P, Schwartz S, Vidal O. 2009. Exhumation Processes in Oceanic and Continental Subduction Contexts: A Review. Subduction Zone Geodynamics: 175–205

Guillot S, Schwartz S, Reynard B, Agard P, Prigent C. 2015. Tectonic significance of serpentinites. Tectonophysics, 646: 1–19

Hacker B R, Abers G A. 2012. Subduction Factory 5: Unusually low Poisson's ratios in subduction zones from elastic anisotropy of peridotite. J Geophys Res: Sol Ea, 117: B06308

Halpaap F, Rondenay S, Ottemöller L. 2018. Seismicity, Deformation, and Metamorphism in the Western Hellenic Subduction Zone: New Constraints From Tomography. J Geophys Res: Sol Ea, 123: 3000–3026

Handy M R, M. Schmid S, Bousquet R, Kissling E, Bernoulli D. 2010. Reconciling plate-tectonic reconstructions of Alpine Tethys with the geological–geophysical record of spreading and subduction in the Alps. Earth-Sci Rev, 102: 121–158

Henry C, Burkhard M, Goffe B. 1996. Evolution of synmetamorphic veins and their wallrocks through a Western Alps transect: no evidence for large-scale fluid flow. Stable isotope, major- and trace-element systematics. Chem Geol, 127: 81–109

Hermann J, Zheng Y F, Rubatto D. 2013. Deep Fluids in Subducted Continental Crust. Elements, 9: 281–287

Huesca-Pérez E, Husker A. 2012. Shallow travel-time tomography below southern Mexico. Geofísica internacional, 51: 281–291

Hunt J D, Manning C E. 2012. A thermodynamic model for the system SiO_2–H_2O near the upper critical end point based on quartz solubility experiments at 500–1100 °C and 5–20 kbar. Geochim Cosmochim Ac, 86: 196–213

Hyndman R D, McCrory P A, Wech A, Kao H, Ague J. 2015. Cascadia subducting plate fluids channelled to fore-arc mantle corner: ETS and silica deposition. J Geophys Res: Sol Ea, 120: 4344–4358

Ji W Q, Malusà M G, Tiepolo M, Langone A, Zhao L, Wu F Y. 2019. Synchronous Periadriatic magmatism in the Western and Central Alps in the absence of slab breakoff.

Terra Nova, 31: 120–128

Komatitsch D, Tromp J. 1991. Introduction to the spectral element method for three-dimensional seismic wave propagation. Geophys J Int, 139: 806–822

Kufner S-K, Schurr B, Sippl C, Yuan X, Ratschbacher L, Akbar A s o M, Ischuk A, Murodkulov S, Schneider F, Mechie J, Tilmann F. 2016. Deep India meets deep Asia: Lithospheric indentation, delamination and break-off under Pamir and Hindu Kush (Central Asia). Earth Planet Sci Lett, 435: 171–184

Li J, Song X. 2021. Crustal structure beneath the Hi-CLIMB seismic array in the central-western Tibetan Plateau from the improved *H-κ-c* method. Earthq Sci, 34: 199–210

Li J, Song X, Wang P, Zhu L. 2019. A Generalized *H-κ* Method With Harmonic Corrections on Ps and Its Crustal Multiples in Receiver Functions. J Geophys Res: Sol Ea, 124: 3782–3801

Li X H, Klyukin Y I, Steele-MacInnis M, Fan H-R, Yang K-F, Zoheir B. 2020. Phase equilibria, thermodynamic properties, and solubility of quartz in saline-aqueous-carbonic fluids: Application to orogenic and intrusion-related gold deposits. Geochim Cosmochim Ac, 283: 201–221

Ligorrfa J P, Ammon C J. 1999. Iterative deconvolution and receiver-function estimation. Bull Seismol Soc Amer, 89: 1395–1400

Liou J G, Tsujimori T, Yang J, Zhang R Y, Ernst W G. 2014. Recycling of crustal materials through study of ultrahigh-pressure minerals in collisional orogens, ophiolites, and mantle xenoliths: A review. J Asian Earth Sci, 96: 386–420

Lowry A R, Perez-Gussinye M. 2011. The role of crustal quartz in controlling Cordilleran deformation. Nature, 471: 353–357

Lu Y, Stehly L, Paul A. 2018. High-resolution surface wave tomography of the European crust and uppermost mantle from ambient seismic noise. Geophys J Int, 214: 1136–1150

Ludwig W J, Nafe J E, Drake C L. 1970. Seismic Refraction, the Sea. Wiley-Interscience, New York, , 4: 53–84

Lyu C, Pedersen H A, Paul A, Zhao L, Solarino S. 2017. Shear wave velocities in the upper mantle of the Western Alps: new constraints using array analysis of seismic surface waves. Geophys J Int, 210: 321–331

Malusà M G, Anfinson O A, Dafov L N, Stockli D F. 2016. Tracking Adria indentation beneath the Alps by detrital zircon U-Pb geochronology: Implications for the Oligocene–Miocene dynamics of the Adriatic microplate. Geology, 44: 155–158

Malusà M G, Faccenna C, Baldwin S L, Fitzgerald P G, Rossetti F, Balestrieri M L, Danišík M, Ellero A, Ottria G, Piromallo C. 2015. Contrasting styles of (U)HP rock exhumation along the Cenozoic Adria-Europe plate boundary (Western Alps, Calabria, Corsica). Geochem Geophys Geosyst, 16: 1786–1824

Malusà M G, Faccenna C, Garzanti E, Polino R. 2011. Divergence in subduction zones and exhumation of high pressure rocks (Eocene Western Alps). Earth Planet Sci

Lett, 310: 21–32

Malusà M G, Guillot S, Zhao L, Paul A, Solarino S, Dumont T, Schwartz S, Aubert C, Baccheschi P, Eva E, Lu Y, Lyu C, Agostinetti N P, Pondrelli S, Salimbeni S, Sun W, Yuan H. 2021. The deep structure of the Alps based on the CIFALPS seismic experiment: A synthesis. Geochem Geophys Geosyst, 22: e2020GC009466

Manning C E. 2004. The chemistry of subduction-zone fluids. Earth Planet Sci Lett, 223: 1–16

Manning C E. 2018. Fluids of the Lower Crust: Deep Is Different. Annu Rev Earth Planet Sci, 46: 67–97

Ni H, Zhang L, Xiong X, Mao Z, Wang J. 2017. Supercritical fluids at subduction zones: Evidence, formation condition, and physicochemical properties. Earth-Sci Rev, 167: 62–71

Nicolas A, Polino R, Hirn A, Nicolich R. 1990b. ECORS-CROP traverse and deep structure of the western Alps: A synthesis. Mémoires de la Société géologique de France, 156: 15–27

Nouibat A, Stehly L, Paul A, Schwartz S, Bodin T, Dumont T, Rolland Y, Brossier R. 2022. Lithospheric transdimensional ambient-noise tomography of W-Europe: implications for crustal-scale geometry of the W-Alps. Geophys J Int, 229: 862–879

Paffrath M, Friederich W, Schmid S M, Handy M R. 2021. Imaging structure and geometry of slabs in the greater Alpine area – a P-wave travel-time tomography using AlpArray Seismic Network data. Solid Earth, 12: 2671–2702

Paul A, Malusà M G, Solarino S, Salimbeni S, Eva E, Nouibat A, Pondrelli S, Aubert C, Dumont T, Guillot S, Schwartz S, Zhao L. 2022. Along-strike variations in the fossil subduction zone of the Western Alps revealed by the CIFALPS seismic experiments and their implications for exhumation of (ultra-) high-pressure rocks. Earth Planet Sci Lett, 598: 117843

Perrier G, Ruegg J C. 1973. Structure profonde du Massif Central Français. Ann Geophys, 29: 435–502

Pettke T, Diamond L W. 1997. Oligocene gold quartz veins at Brusson, NW Alps: Sr isotopes trace the source of ore-bearing fluid to over a 10-km depth. Econ Geol, 92: 389–406

Rapp J F, Klemme S, Butler I B, Harley S L. 2010. Extremely high solubility of rutile in chloride and fluoride-bearing metamorphic fluids: An experimental investigation. Geology, 38: 323–326

Reynard B. 2013. Serpentine in active subduction zones. Lithos, 178: 171–185

Salimbeni S, Malusà M G, Zhao L, Guillot S, Pondrelli S, Margheriti L, Paul A, Solarino S, Aubert C, Dumont T, Schwartz S, Wang Q, Xu X, Zheng T, Zhu R. 2018. Active and fossil mantle flows in the western Alpine region unravelled by seismic anisotropy analysis and high-resolution P wave tomography. Tectonophysics, 731–732: 35–47

Schneider F M, Yuan X, Schurr B, Mechie J, Sippl C, Haberland C, Minaev V, Oimahmadov I, Gadoev M, Radjabov N, Abdybachaev U, Orunbaev S, Negmatullaev S. 2013. Seismic imaging of subducting continental lower crust beneath the Pamir. Earth

Planet Sci Lett, 375: 101–112

Shiranzaei G, Nasrabadi A, Sepahvand M. 2021. Moho depth variations and Vp/Vs ratio in the Zagros (Iran) from teleseismic converted waves. J Seismol, 25: 671–682

Solarino S, Malusà M G, Eva E, Guillot S, Paul A, Schwartz S, Zhao L, Aubert C, Dumont T, Pondrelli S, Salimbeni S, Wang Q, Xu X, Zheng T, Zhu R. 2018. Mantle wedge exhumation beneath the Dora-Maira (U)HP dome unravelled by local earthquake tomography (Western Alps). Lithos, 296–299: 623–636

Spada M, Bianchi I, Kissling E, Agostinetti N P, Wiemer S. 2013. Combining controlled-source seismology and receiver function information to derive 3-D Moho topography for Italy. Geophys J Int, 194: 1050–1068

Stern R J. 2002. Subduction Zones. Rev Geophys, 40: 3-1–3-38

Sun W, Zhao L, Malusà M G, Guillot S, Fu L. 2019. 3-D Pn tomography reveals continental subduction at the boundaries of the Adriatic microplate in the absence of a precursor oceanic slab. Earth Planet Sci Lett, 510: 131–141

Talwani M, Worzel J L, Landisman M. 1959. Rapid gravity computations for two-Dimensional Bodies with Application to the Mendocino Submarine Fracture Zone. J Geophys Res, 64: 49–59

Tricart P, Schwartz S, Sue C, Lardeaux J-M. 2004. Evidence of synextension tilting and doming during final exhumation from analysis of multistage faults (Queyras Schistes lustrés, Western Alps). Journal of Structural Geology, 26: 1633–1645

Wang X, Kaus B J P, Yang J, Wang K, Li Y, Chen L, Zhao L. 2021. 3D Geodynamic Models for HP-UHP Rock Exhumation in Opposite-Dip Double Subduction-Collision Systems. J Geophys Res: Sol Ea, 126: e2021JB022326

Wen L, Helmberger D V. 1998. A two-dimensional P-SV hybrid method and its application to modeling localized structures near the core-mantle boundary. J Geophys Res: Sol Ea, 103: 17901–17918

Zahorec P, Papčo J, Pašteka R, Bielik M, Bonvalot S, Braitenberg C. 2021. The first pan-Alpine surface-gravity database, a modern compilation that crosses frontiers. Earth Syst Sci Data, 13: 2165–2209

Zhao L, Malusà M G, Yuan H, Paul A, Guillot S, Lu Y, Stehly L, Solarino S, Eva E, Lu G, Bodin T. 2020. Evidence for a serpentinized plate interface favouring continental subduction. Nat Commun, 11: 2171

Zhao L, Paul A, Guillot S, Solarino S, Malusà M G, Zheng T, Aubert C, Salimbeni S, Dumont T, Schwartz S, Zhu R, Wang Q. 2015. First seismic evidence for continental subduction beneath the Western Alps. Geology, 43: 815–818

Zhao L, Paul A, Malusà M G, Xu X, Zheng T, Solarino S, Guillot S, Schwartz S, Dumont T, Salimbeni S, Aubert C, Pondrelli S, Wang Q, Zhu R. 2016. Continuity of the Alpine slab unraveled by high-resolution P wave tomography. J Geophys Res: Sol Ea, 121: 8720–8737

Zhao L, Wen L, Chen L, Zheng T. 2008. A two-dimensional hybrid method for modeling seismic wave propagation in anisotropic media. J Geophys Res, 113: B12307

Zheng T, He Y, Ding L, Jiang M, Ai Y, Mon C T, Hou G, Sein K, Thant M. 2020. Direct structural evidence of Indian continental subduction beneath Myanmar. Nat Commun, 11: 1944

Zheng Y-F, Zhao Z-F, Chen R-X. 2019. Ultrahigh-pressure metamorphic rocks in the Dabie–Sulu orogenic belt: compositional inheritance and metamorphic modification. Geological Society, London, Special Publications, 474: 89–132

Zheng Y, Chen R, Xu Z, Zhang S. 2016. The transport of water in subduction zones. Sci China Earth Sci, 59: 651–682

Zheng Y, Hermann J. 2014. Geochemistry of continental subduction-zone fluids. Earth Planets Space, 66: 93

Zheng Y F, Chen Y X. 2016. Continental versus oceanic subduction zones. Natl Sci Rev, 3: 495–519

Zhu L, Kanamori H. 2000. Moho depth variation in southern California from teleseismic receiver functions. J Geophys Res: Sol Ea, 105: 2969–2980

Acknowledgments

We are grateful to the very extensive discussions and comments on the manuscript by Anne Paul. We also appreciate the valuable comments and suggestions provided by several anonymous reviewers that greatly improved the quality of this manuscript, and we appreciate the assistance provided by the editors of SCIENCE CHINA Earth Sciences in facilitating the publication of this article. We sincerely thank Jiangtao Li for sharing the Himalaya crustal thickness and *V*p/*V*s results of Hi-Climb experiment. And we also greatly appreciate the several discussions with Huaiyu Yuan and Jianfeng Yang. The raw data of the two CIFALPS projects were provided by the data centers of the IGGCAS (Institute of Geology and Geophysics, Chinese Academy of Sciences) and the RESIF (French seismic and geodetic network). We also used records of permanent networks and of the AlpArray seismic network.

Funding: This work is funded by the National Natural Science Foundation of China (Grant 41888101).

Author contributions:

Conceptualization: LZ

Methodology: LZ, YM

Investigation: YM, MM, LZ, BS

Visualization: YM, BS, MM

Writing —original draft: YM

Writing —review: LZ, MM, SS, SP, CA, SS, EE, SG

Competing interests: The authors declare that they have no competing interest.